Supplement of Earth Syst. Dynam., 17, 607–630, 2026
https://doi.org/10.5194/esd-17-607-2026-supplement

Supplement of

Assessing the performance of LPJmL-5 in simulating vegetation responses to normal and multi-year droughts

Denise Ruijsch et al.

Correspondence to: Denise Ruijsch (d.ruijsch@uu.nl)

Contents of this file

S1 PET and SPEI calculation

The calculation of the Standardized Precipitation Evapotranspiration Index (SPEI) requires both precipitation (P) and potential evapotranspiration (PET) data. Precipitation data were obtained directly from the W5E5 dataset, while PET was computed separately using several W5E5 climate variables, including total precipitation (tp), surface temperature (tas), sea level pressure (ps), surface wind speed (sfcwind), daily mean relative humidity (hurs), and surface downwelling shortwave radiation (rsds). The W5E5 dataset provides these variables at a daily temporal resolution and a spatial resolution of 0.5° (Lange et al., 2022).

PET was calculated using the Penman-Monteith (FAO56) method (Monteith, 1965; Zotarelli et al., 2024), implemented via the pyet package in Python (Vremec et al., 2023):

$$PET = \frac{0.408\Delta(Rn - G) + \gamma\frac{900}{T+273}u_2(e_s - e_a)}{\Delta + \gamma(1 + 0.34u_2)} \tag{S1}$$

The SPEI is derived from the climatic water balance (D), defined as the difference between monthly precipitation and PET (measured in mm/month) (Vicente-Serrano et al., 2010):

$$D = P - PET \tag{S2}$$

Climatic water balance values were aggregated over timescales from 1 to 24 months. A log-logistic distribution was then fitted to the aggregated water balance time series over a calibration period spanning 1950 to 2019. This enabled the computation of SPEI values for different timescales (SPEI-1 through SPEI-24). For each focus region, the spatial averages of precipitation and PET were calculated prior to calculating the climatic water balance and deriving the SPEI-12 time series for that region.

S2 SPEI as a drought indicator

To verify that droughts identified using the SPEI-12 correspond to actual reductions in soil water availability, we analysed Soil Water Content (SWC) from the LPJmL-5 simulations. This analysis focused on the energy-limited region of northern Europe (10°W–40°E, 50–70°N).

For each drought identified using SPEI, we calculated the mean SWC expressed as a percentage of historical saturation within the drought period, calculated as $\mathrm{SWC_{sat}} = \frac{\mathrm{SWC}-\mathrm{SWC_{min}}}{\mathrm{SWC_{max}}-\mathrm{SWC_{min}}} \times 100\%$, and compared it to the mean SWC during near-normal conditions (Table S1). Across all five soil layers, SWC during droughts was consistently lower than during near-normal periods, with reductions ranging from approximately 4% to 9%. This confirms that negative SPEI values also reflect reductions in water availability.

Table S1. Soil water content (SWC) expressed as percent of historical saturation during droughts (SPEI < -1) and near-normal conditions (-0.5 < SPEI < 0.5) across five soil layers for northern Europe (10°W–40°E, 50–70°N). Reductions of approximately 4–9% indicate a decrease in water availability during drought periods compared to normal periods.

Soil layer	SWC during droughts (%)	SWC during normal periods (%)	Reduction (%)
SWC1	78.3	82.0	3.7
SWC2	71.2	77.3	6.1
SWC3	69.8	75.8	6.0
SWC4	44.6	48.9	4.3
SWC5	10.4	19.1	8.7

Figure S1 shows the mean SWC anomaly for the 1959–1960 MYD in northern Europe across the five soil layers. Soil water availability was consistently lower during this drought, further confirming that negative SPEI values correspond to actual reductions in water availability.

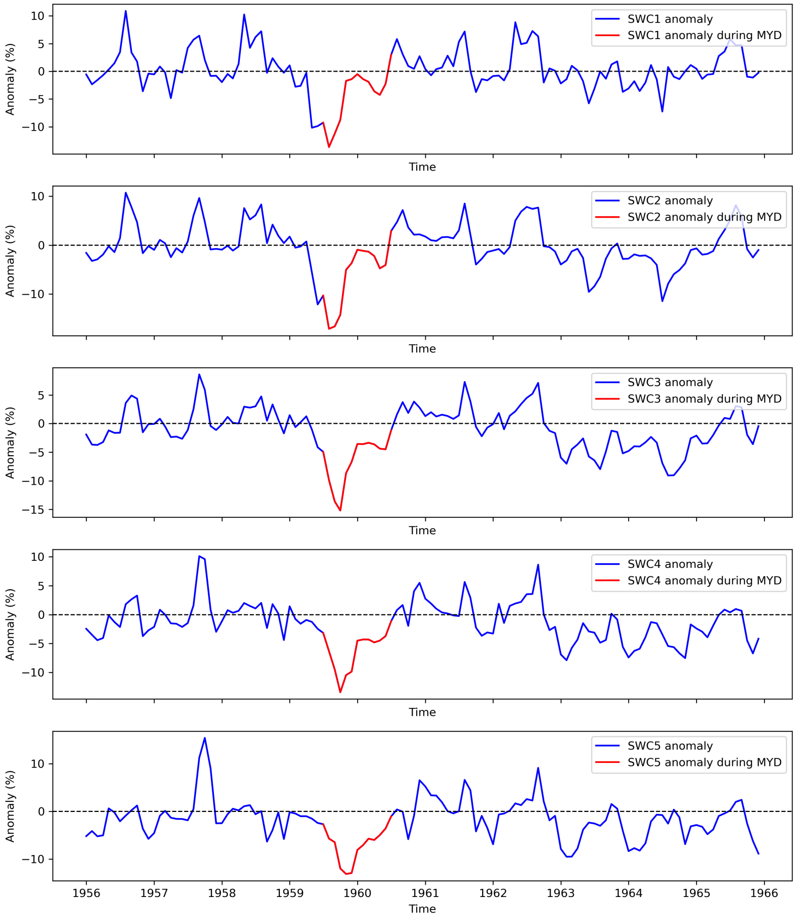

Figure S1. Mean soil water content (SWC) anomaly during the 1959–1960 MYD in northern Europe across five soil layers. The blue line shows the SWC anomalies for each layer, while the orange line indicates the identified MYD period. Negative anomalies reflect reduced soil water availability during the drought.

S3 MODIS GPP as a validation dataset

Because we use MODIS GPP to evaluate LPJmL5 GPP, it is important to first assess how it represents vegetation productivity. MODIS GPP is not a purely observational dataset, but rather satellite-derived using the MOD17 light-use efficiency algorithm (Running and Zhao, 2021). Key inputs include MODIS Fraction of Absorbed Photosynthetically Active Radiation (FPAR), meteorological data (temperature and vapor pressure deficit), and MODIS land-cover classification (Running and Zhao, 2021). To evaluate its suitability as a validation dataset, we therefore compare MODIS GPP with two satellite products that are more directly observation-based: the MODIS Enhanced Vegetation Index (EVI; Didan (2015a, b)) and the solar-induced chlorophyll fluorescence (SIF; Wang and Zhang (2023)).

Previous work assessing vegetation responses to multi-year droughts (MYDs) relied primarily on EVI (Ruijsch et al., 2025). Because EVI and GPP originate from the same sensor, this comparison allows us to examine which differences arise from the MOD17 algorithm itself.

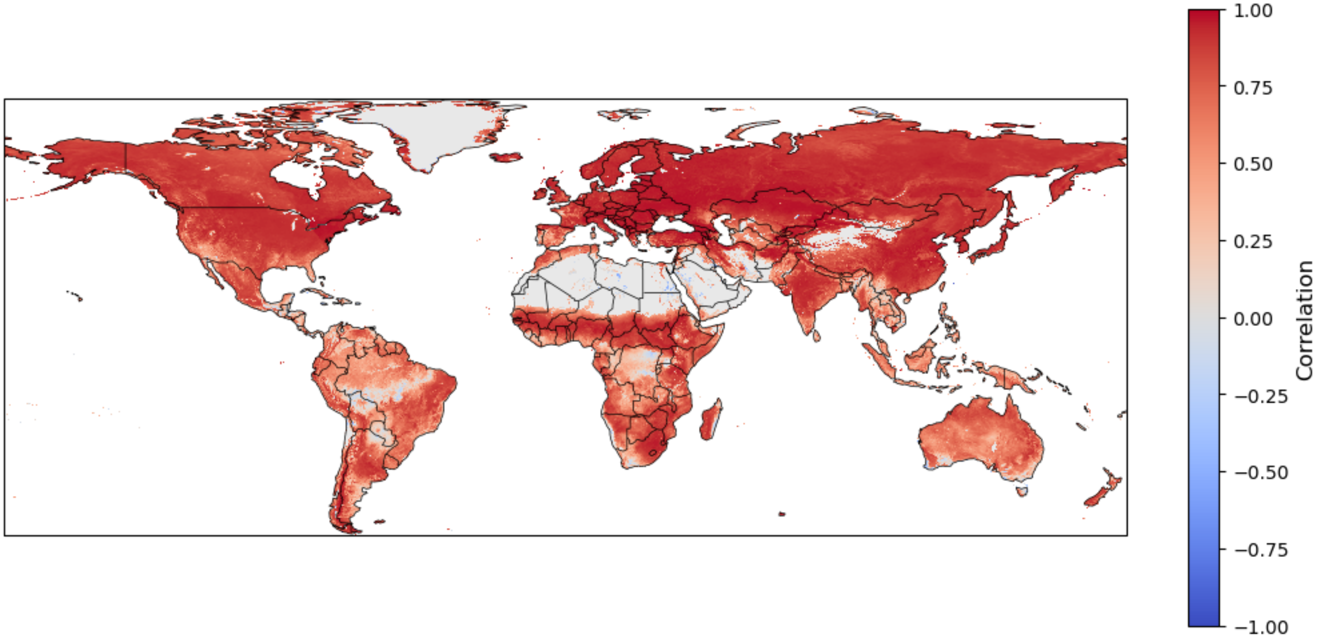

Figure S2. Spearman correlation between MODIS EVI and GPP products (2000-02 until 2023-02).

We calculated the Spearman correlation between MODIS EVI and GPP for February 2000–February 2023 (Figure S2) and found a strong positive correlation, especially in the Northern Hemisphere ($EVI = 0.86 \cdot GPP$; $R^2 = 0.57$; $\rho = 0.76, p < 0.001$). This indicates that both products capture broadly similar vegetation dynamics. Correlations are lower in parts of the tropics and Southern Hemisphere. Nevertheless, Ruijsch et al. (2025) found that MODIS GPP and EVI show comparable responses to MYDs when using standardized anomalies, suggesting that MODIS GPP is adequate for our purposes. Ruijsch et al. (2025) further found similar consistency when comparing the Leaf Area Index (LAI) to the GPP during MYDs.

To further assess MODIS GPP, we compared it with SIF (Figure S3). We found an overall positive relationship ($SIF = 0.41 \cdot GPP$; $R^2 = 0.21$; $\rho = 0.50, p < 0.001$). Correlations are highest across temperate and boreal regions and weaker or negative in parts of the tropics, consistent with findings by Tang et al. (2015). Overall, this supports that MODIS GPP captures large-scale variation in photosynthetic activity, while also highlighting regional limitations.

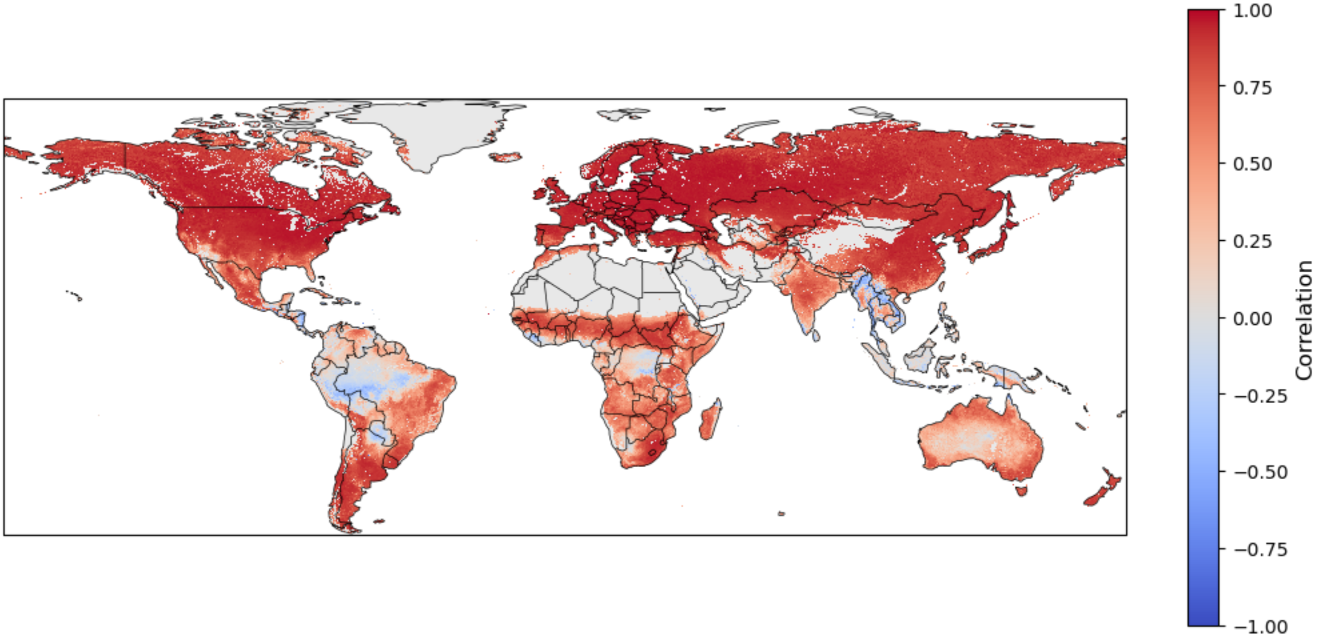

Figure S3. Spearman correlation between MODIS GPP and SIF products (2000-02 until 2018-12).

Several studies validating the MODIS GPP have been done, where they report reasonable performance in general, with most errors linked to input datasets rather than the algorithm itself. Tang et al. (2015) found MODIS GPP performs well across temperate and mixed forests but less so in evergreen broadleaf forests, particularly in the tropics. Wang et al. (2017) showed that much of the error originates from FPAR, land-cover misclassification, and light-use efficiency parameters rather than meteorology. Zhu et al. (2018) reported systematic underestimation in grasslands (≈34%), with better performance in lower-productivity systems. These studies agree that cloud contamination and uncertainties in tropical regions remain key challenges.

Taken together, the strong correspondence between MODIS GPP, EVI, and SIF indicates that MODIS GPP provides a biologically meaningful representation of vegetation productivity. We therefore use MODIS GPP as our validation dataset for LPJmL5 GPP, while acknowledging that performance is weaker in tropical ecosystems and results should be interpreted with these limitations in mind.

S4 Differences in input and setup in LPJmL-5

Modelled GPP in LPJmL-5 is influenced by choices in input data and setup. In this study, we examine two key aspects: (i) the effect of different radiation input configurations, and (ii) the impact of using ERA5 (Hersbach et al., 2023) versus W5E5 (Lange et al., 2022) meteorological forcing. Both factors can significantly alter simulated GPP and affect the magnitude and spatial patterns of vegetation responses to drought.

S4.1 Radiation input

To assess the impact of radiation input on model performance, LPJmL-5 simulations were conducted at a 0.5° spatial resolution using ERA5 climate data (Hersbach et al., 2023). In this study we tested the three radiation configurations of LPJmL-5: (1) cloudiness-based radiation, (2) shortwave downward radiation only, and (3) combined shortwave and longwave downward radiation. Figures S4 and S5 indicate that simulations using cloudiness-based radiation consistently produce lower GPP values compared to longwave and shortwave combined, with the largest differences observed in tropical regions. Using only shortwave radiation, rather than both longwave and shortwave, also results in lower GPP globally than shortwave and longwave combined. This suggests that the choice of radiation input can significantly influence modeled vegetation productivity, particularly in areas with high solar radiation. Based on these results, we use the combined longwave and shortwave radiation setting in all subsequent simulations to ensure more consistent and accurate estimates of GPP.

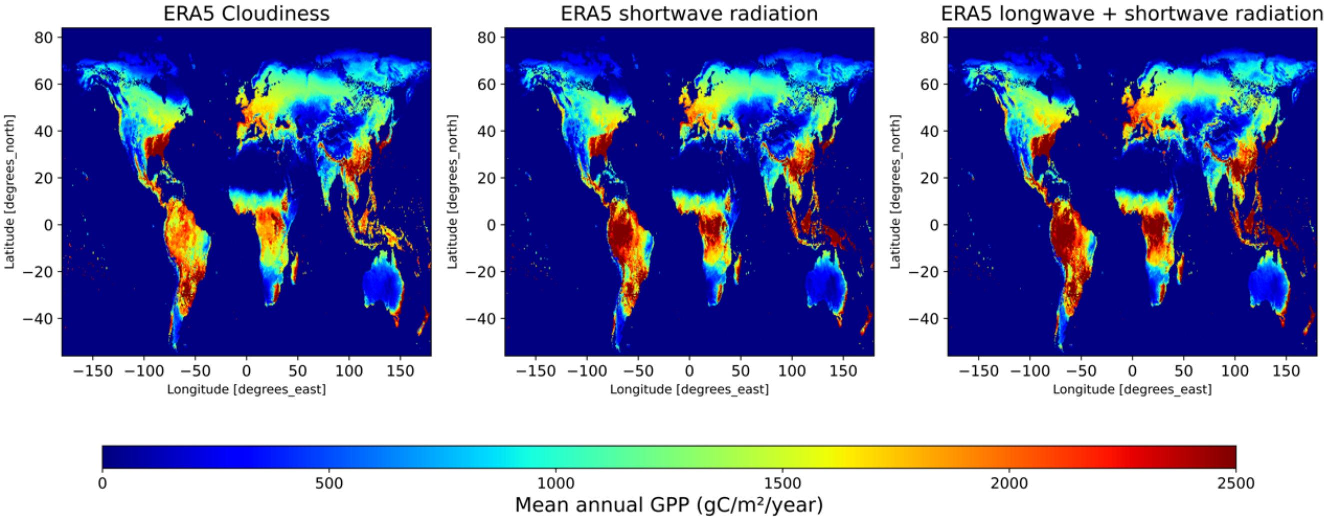

Figure S4. Comparison of mean annual GPP (2000–2019) simulated with LPJmL-5 using cloudiness-based, shortwave-only, and combined longwave + shortwave radiation inputs.

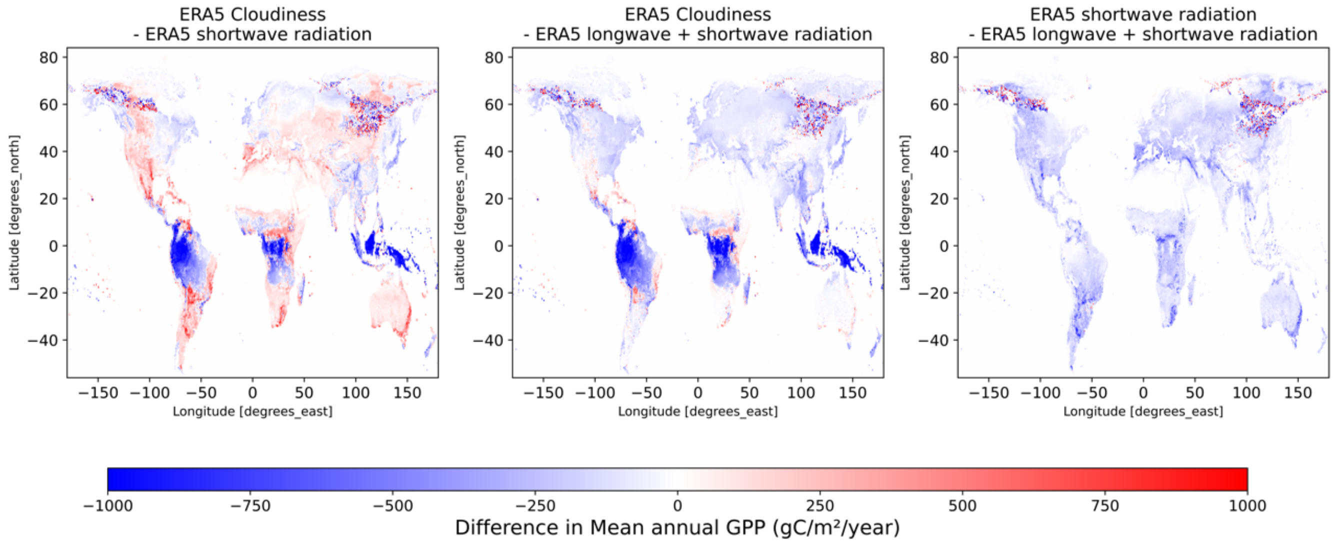

Figure S5. Difference in mean annual GPP (2000–2019) simulated with LPJmL-5 across cloudiness-based, shortwave-only, and combined longwave + shortwave radiation inputs.

S4.2 ERA5 vs W5E5 as input for LPJmL-5

In this study, both ERA5 (Hersbach et al., 2023) and W5E5 (Lange et al., 2022) were used for the calculation of SPEI and as input for LPJmL-5. ERA5 provides hourly reanalysis data from 1940 to the present, while W5E5 is a bias-corrected version of ERA5 available at daily resolution from 1901–2019. The earlier study by Ruijsch et al. (2025) relied on ERA5, which is convenient with the shorter MODIS time range (2000-present). In contrast, this study aims to extend the analysis further back in time, making W5E5 the more suitable choice. To allow for a direct comparison between the two studies, however, we first evaluate whether ERA5 and W5E5 produce consistent MYD periods.

Figure S6 shows the number of MYDs between 2000–2019 based on SPEI-12 calculated from monthly W5E5 and ERA5. Using W5E5 generally results in fewer MYDs, particularly in the tropics, reflecting regional biases in ERA5 that are partially corrected in W5E5. Fewer MYDs are also found in Argentina, northern Europe, and parts of Asia when using W5E5. However, in this study we mostly focus on the effect of MYDs in our six defined focus regions. Looking at the SPEI-12 timeseries in those regions (Figure S7), we can see that all ERA5 MYD periods are also present in the W5E5 dataset, with the exception of the 2004 MYD in WEU. This leads us to believe that changing from ERA5 in previous research to W5E5 now will not significantly affect the identified MYD periods in the focus regions.

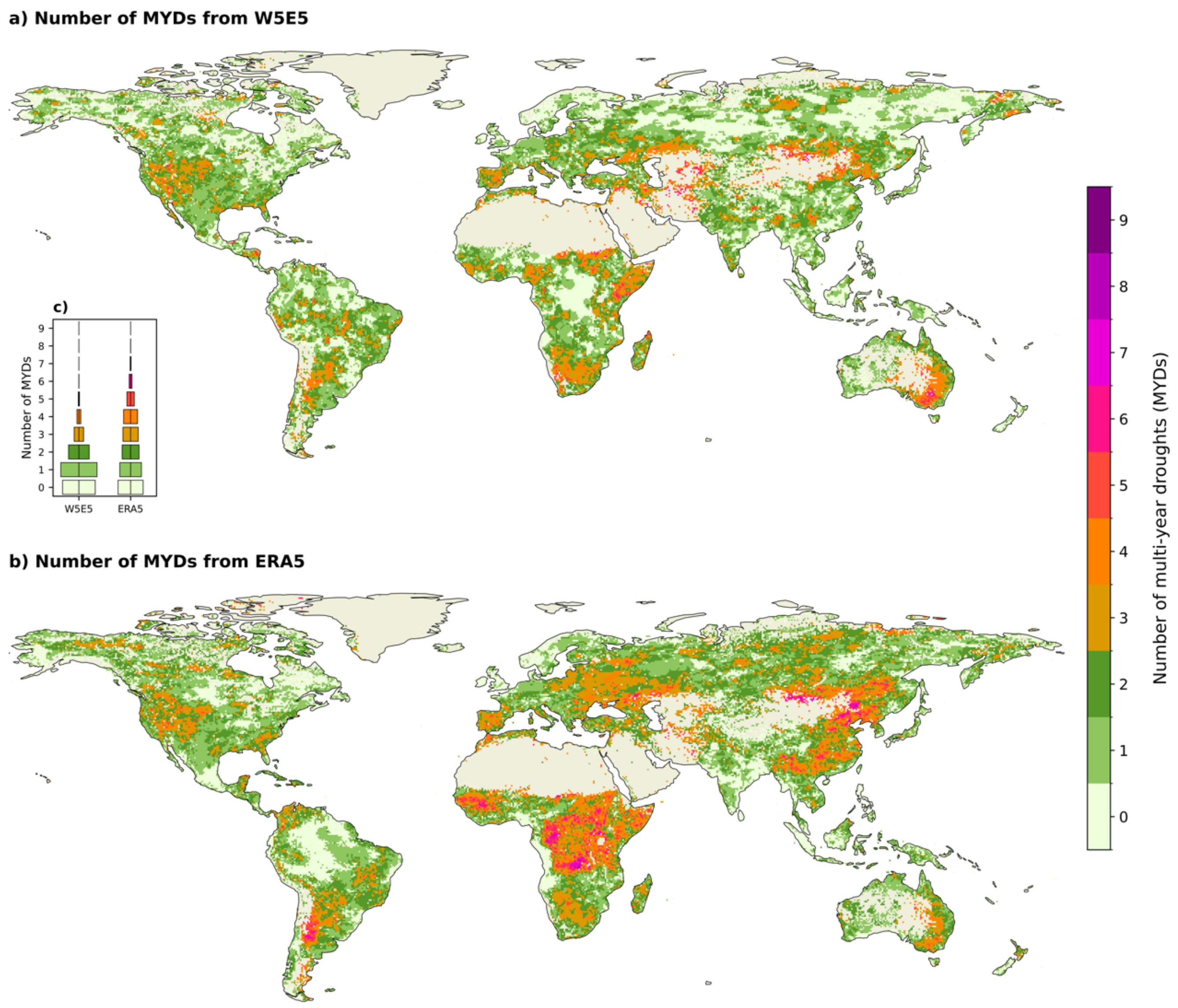

Figure S6. Comparison of the number of MYDs (2000-2019) calculated from ERA5 and W5E5 SPEI-12. c) shows violin plots of both.

Figure S8 presents the mean annual GPP (2000–2019) simulated by LPJmL-5 using ERA5 (monthly) and W5E5 (monthly and daily) climate inputs. Figure S9 shows the differences between these simulations.

Some notable differences appear between the ERA5 monthly and W5E5 daily simulations, which can be attributed to both dataset differences and temporal resolution effects. To disentangle these factors, we first compare W5E5 monthly versus ERA5 monthly inputs (shown in the first plot). This comparison primarily reflects the impact of bias correction, with some regions showing GPP differences of up to 1000 gC/m^2/year.

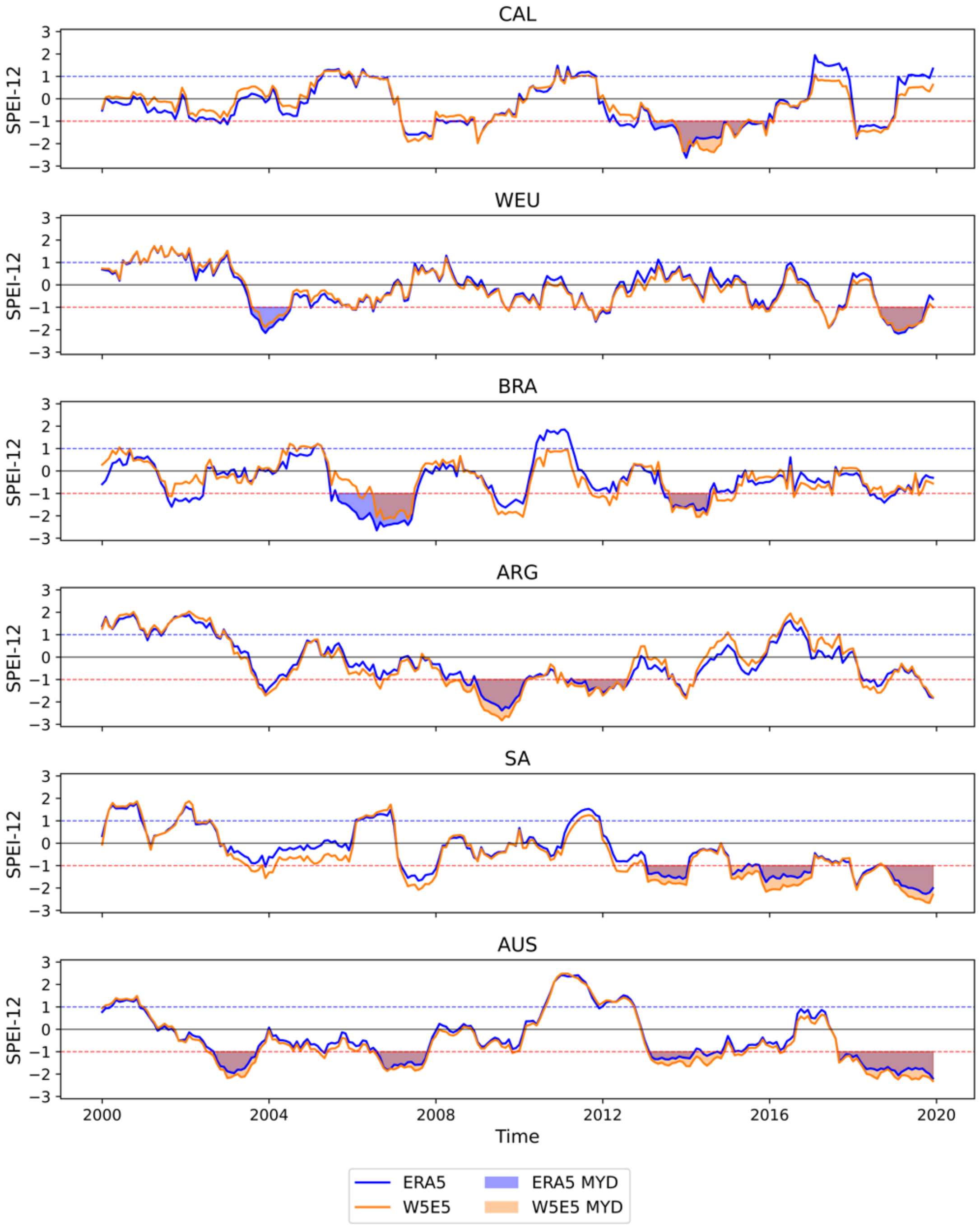

Figure S7. Comparison of SPEI-12 calculated from ERA5 and W5E5 for the six selected focus regions (2000-2019). Blue line is ERA5 and orange line is W5E5. Shaded areas are the MYDs.

Next, we compare W5E5 monthly versus daily inputs within LPJmL-5 simulations to isolate the effect of temporal resolution (shown in the third plot). This comparison reveals that GPP tends to be higher with monthly input in energy-limited regions, while daily input produces higher GPP in water-limited regions. These differences arise because temporal resolution influences how variability affects water availability and energy constraints. In water-limited regions, daily rainfall events reduce stress and boost GPP, whereas monthly averages smooth out this variability, lowering GPP. In energy-limited regions, monthly averages provide more stable conditions that support higher GPP, while daily inputs capture short-term fluctuations that can temporarily reduce GPP.

For this study, we chose W5E5 over ERA5 due to its bias corrections, which provide more accurate climate forcing data. We specifically selected the daily W5E5 input because the higher temporal resolution better captures precipitation variability, especially in water-limited regions. This enables LPJmL-5 to simulate vegetation responses more realistically by representing intermittent rainfall events and short-term drought relief that monthly averages tend to smooth out.

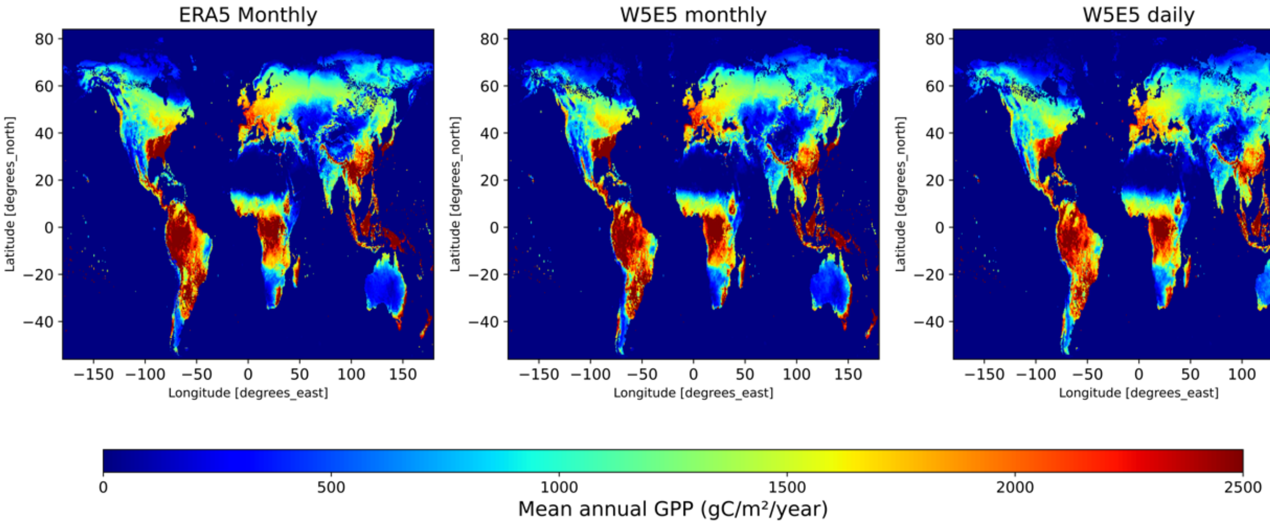

Figure S8. Comparison of mean annual GPP (2000-2019) calculated with LPJmL-5 with ERA5 (monthly) and W5E5 (monthly and daily) input.

S5 LPJmL-5 dynamic landcover vs ESA landcover

In LPJmL-5, vegetation can either be simulated dynamically or prescribed based on observed land cover. Using dynamic land cover can lead to mismatches between modelled and actual vegetation distributions, which may influence the accuracy of GPP simulations. To address this and ensure that the vegetation input aligns more closely with observed land cover, we created a prescribed land cover map based on the 2019 ESA dataset.

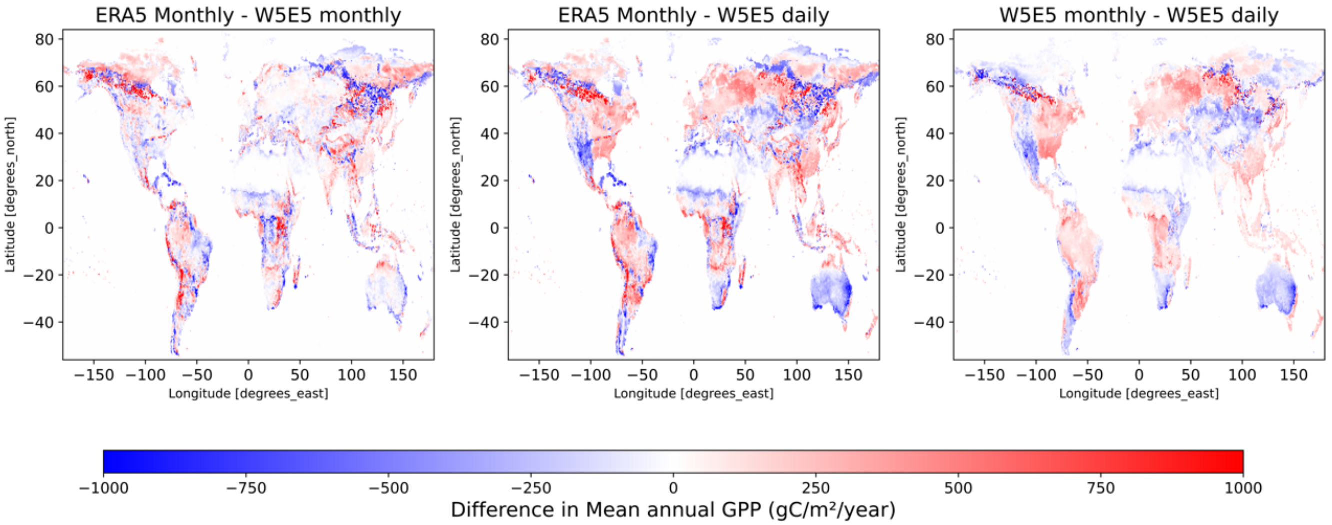

Figure S9. Difference in mean annual GPP (2000-2019) calculated with LPJmL-5 with ERA5 (monthly) and W5E5 (monthly and daily) input.

S5.1 Creating the ESA-Based Landcover Fraction Map

For the land cover input, we used PFT maps from Harper et al. (2023), which provide fractional cover of tree, shrub, and grass types. Because LPJmL classifies Plant Functional Types (PFTs) according to climate zones (tropical, temperate, boreal), we reclassified the ESA PFTs into LPJmL-compatible PFTs using the Köppen–Geiger climate classification (Beck et al., 2023), following the methodology of Forkel et al. (2019) (Table S2). Shrubs were merged with the corresponding tree PFTs since LPJmL does not distinguish between these growth forms.

S5.2 Comparison Between dynamic LPJmL-5 landcover and prescribed ESA Landcover

To assess potential mismatches in vegetation distribution, we compared landcover outputs from LPJmL-5 with observed vegetation cover from the ESA dataset. Notable differences are evident in regions such as Western Europe and parts of South Africa, where LPJmL-5 simulates temperate needleleaved evergreen forests, while ESA data indicates predominantly temperate grasslands.

Globally, the ESA dataset shows greater coverage of temperate and polar C3 grasses, as well as boreal needleleaved summergreen forests. In contrast, LPJmL-5's dynamic vegetation simulates more temperate needleleaved evergreen trees, boreal needleleaved evergreen trees, boreal broadleaved summergreen trees, and tropical C4 grasses.

These discrepancies highlight the importance of aligning vegetation distributions when validating model output against observations. Therefore, we decided to use prescribed ESA-based landcover fractions in the main analysis to ensure consistency between modeled and observed vegetation patterns.

Table S2. Mapping of ESA land cover types to LPJmL Plant Functional Types (PFTs), based on Köppen climate zones following Forkel et al. (2019).

LPJmL PFT	Mapped ESA Land Cover Types	Climate Zone (Köppen Codes)
Tropical broadleaved evergreen tree	TREES-BE, SHRUBS-BE	Tropical (1–3)
Tropical broadleaved raingreen tree	TREES-BD, SHRUBS-BD	Tropical (1–3)
Temperate needleleaved evergreen tree	TREES-NE, SHRUBS-NE	Temperate (4–18, 21, 22, 25, 26)
Temperate broadleaved evergreen tree	TREES-BE, SHRUBS-BE	Temperate (4–18, 21, 22, 25, 26)
Temperate broadleaved summergreen tree	TREES-BD, SHRUBS-BD	Temperate (4–18, 21, 22, 25, 26)
Boreal needleleaved evergreen tree	TREES-NE, SHRUBS-NE	Boreal (19–20, 23–24, 27–30)
Boreal broadleaved summergreen tree	TREES-BD, SHRUBS-BD	Boreal (19–20, 23–24, 27–30)
Boreal needleleaved summergreen tree	TREES-ND, SHRUBS-ND	Boreal (19–20, 23–24, 27–30)
Tropical C4 grass	GRASS-NAT	Tropical (1–3)
Temperate C3 grass	GRASS-NAT	Temperate (4–18, 21, 22, 25, 26)
Polar C3 grass	GRASS-NAT	Boreal (19–20, 23–24, 27–30)

S5.3 Differences in GPP Due to Landcover Settings

To assess the impact of different landcover settings on simulated GPP, we compared LPJmL-5 simulations using dynamic versus prescribed (ESA-based) landcover settings. Figure S13 shows the mean annual GPP (2000–2019) for both configurations. The results highlight clear spatial differences in GPP, particularly in regions where LPJmL-5 dynamic vegetation differs substantially from observed landcover (e.g., parts of Europe and southern Africa). This demonstrates how mismatches in vegetation type can directly influence modelled GPP and highlights the importance of using observed landcover when evaluating model performance.

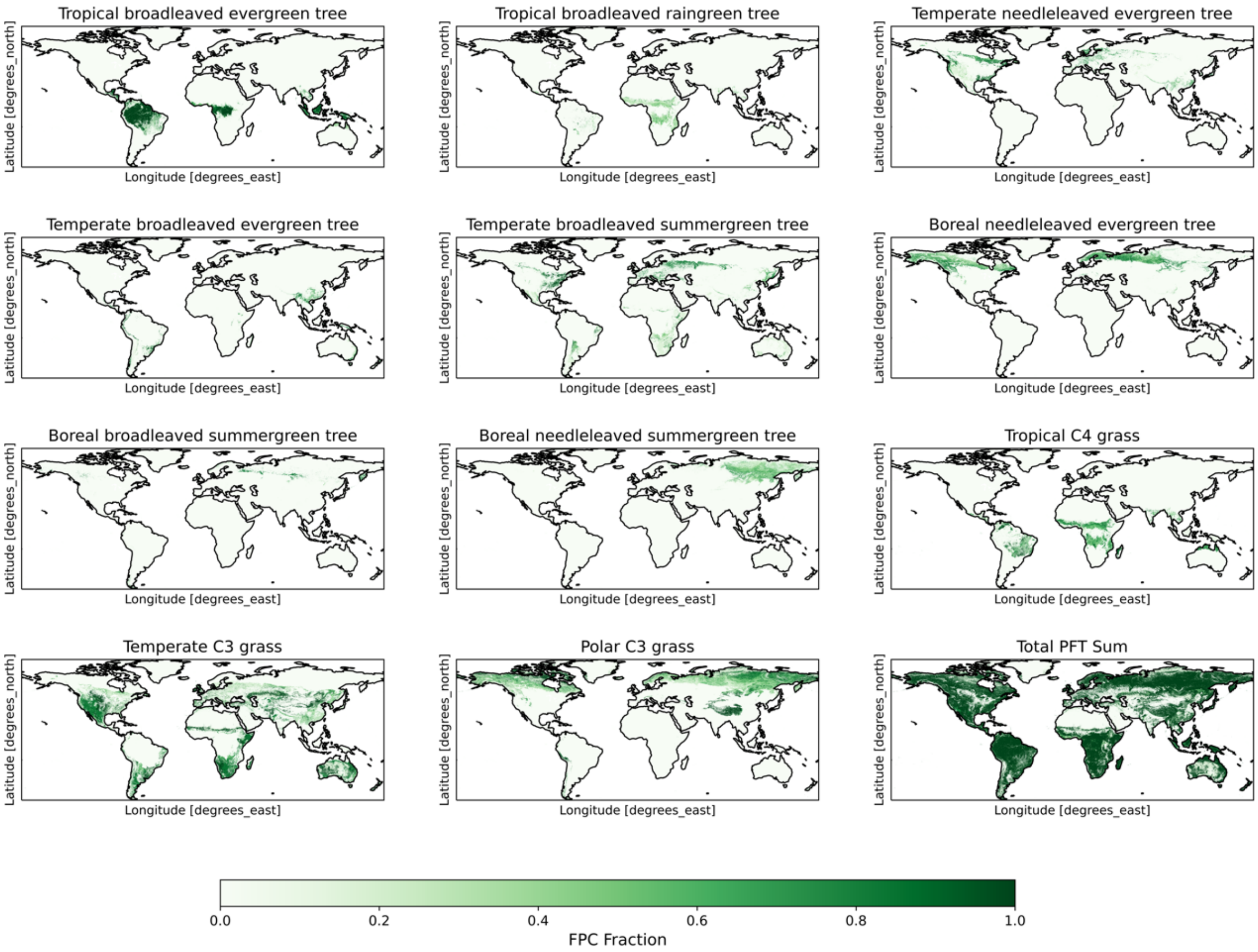

Figure S10. Vegetation cover fractions from the ESA Land Cover dataset (2019) for each PFT and the total PFT sum.

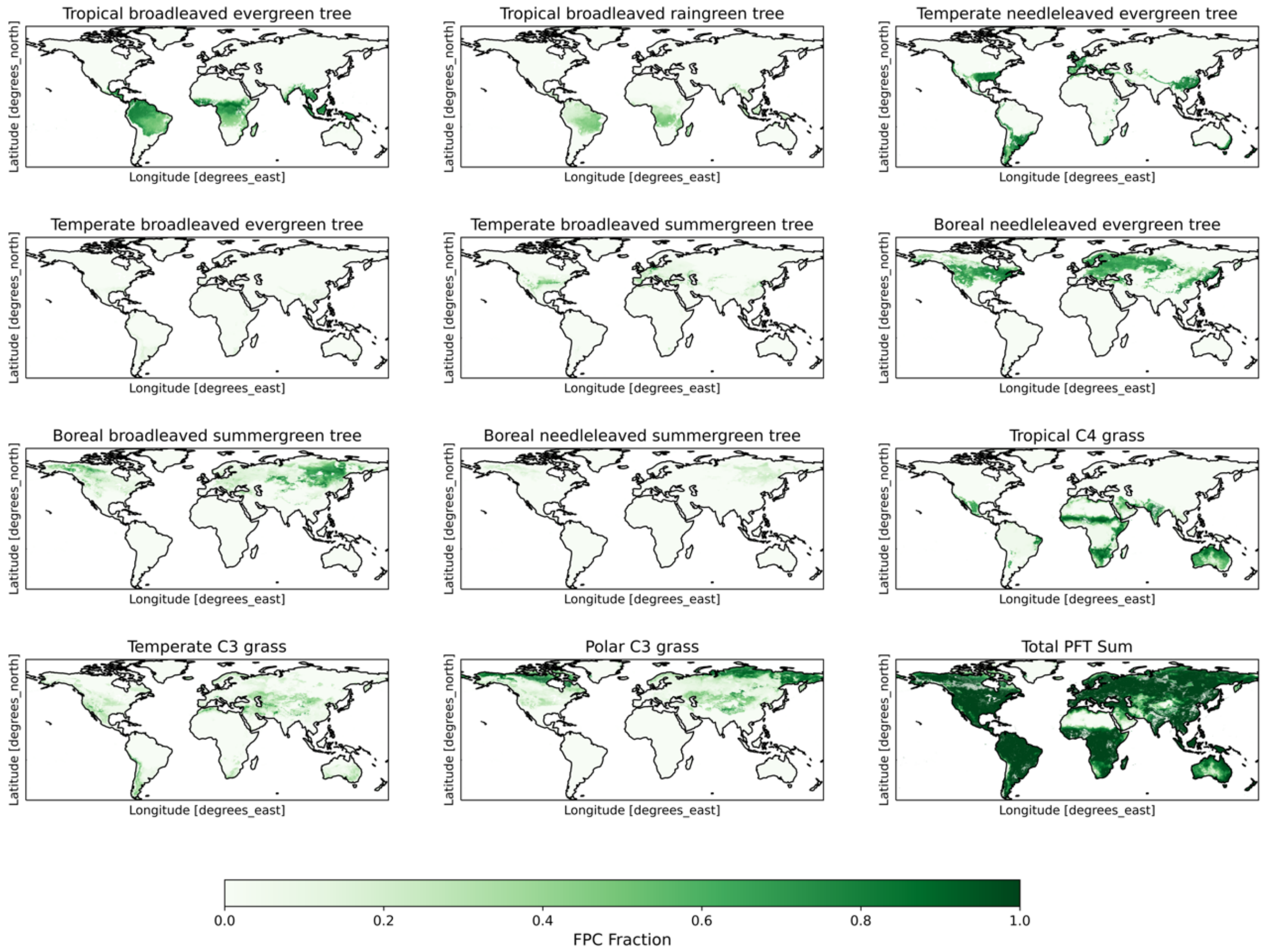

Figure S11. Vegetation cover fractions simulated by LPJmL-5 using dynamic vegetation for each PFT and the total PFT sum..

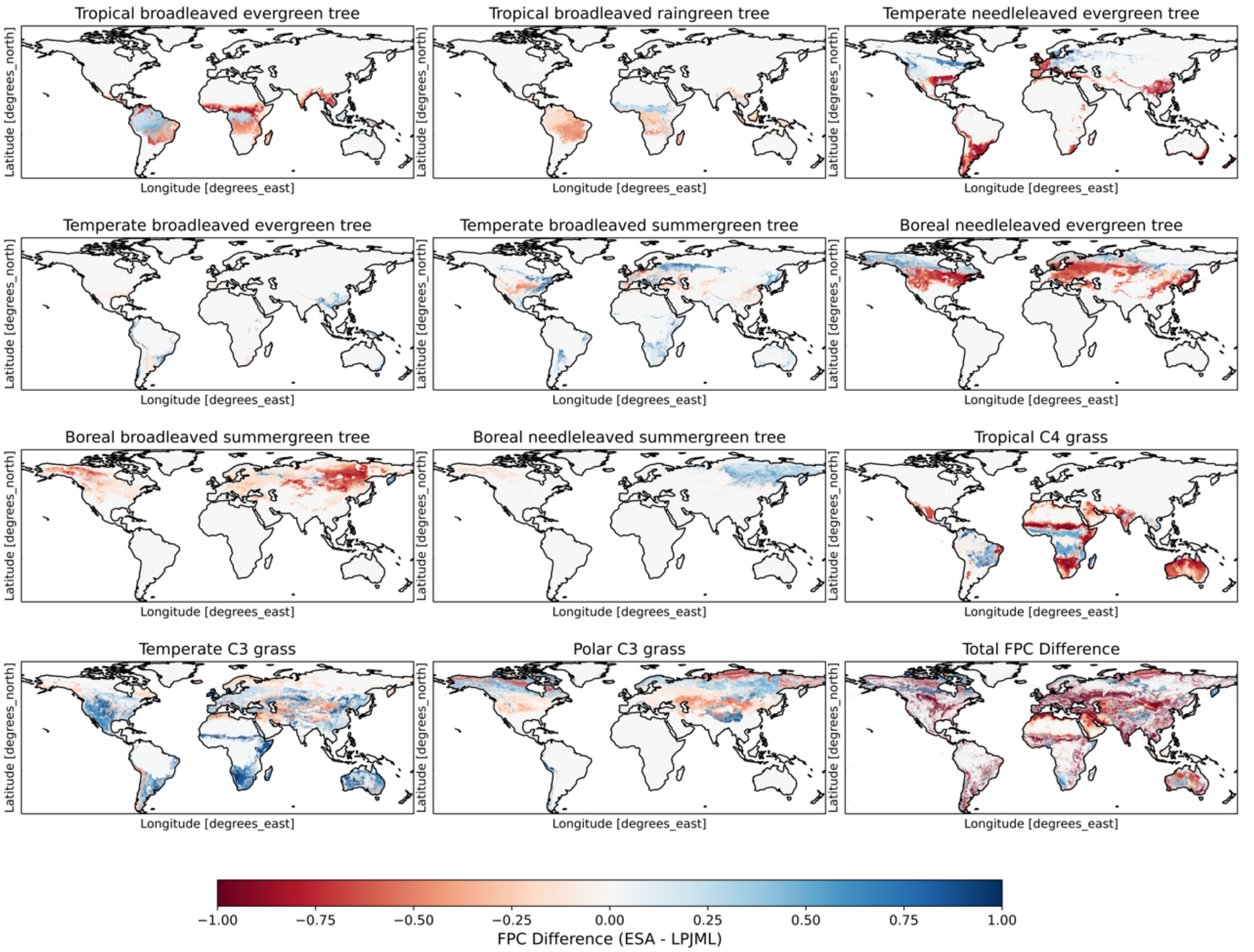

Figure S12. Difference in vegetation cover fractions between LPJmL-5 and ESA. Blue areas indicate where ESA has a higher vegetation fraction; red areas indicate where LPJmL-5 simulates a higher vegetation fraction.

145

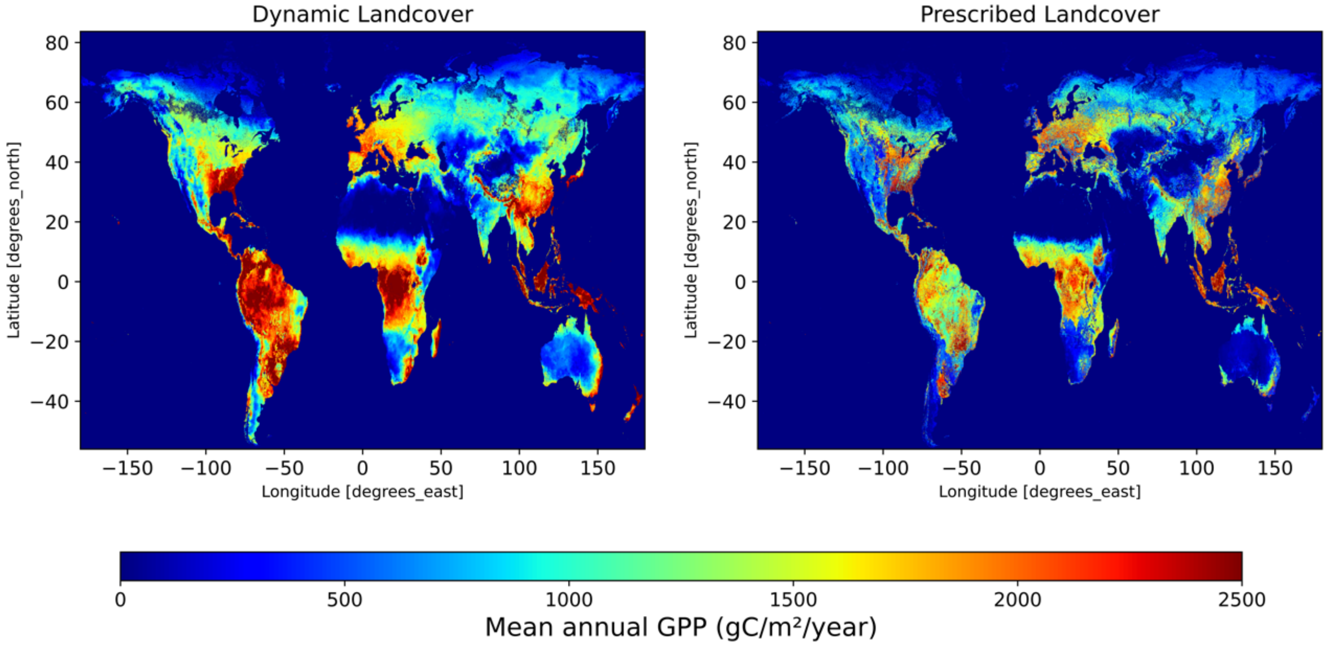

Figure S13. Comparison of mean annual GPP (2000–2019) simulated by LPJmL-5 using dynamic versus prescribed (ESA) landcover.

References

Beck, H., McVicar, T., Vergopolan, N., Berg, A., Lutsko, N., Dufour, A., Zeng, Z., Jiang, X., van Dijk, A., and Miralles, D.: High-resolution (1 km) Köppen-Geiger maps for 1901–2099 based on constrained CMIP6 projections, Scientific Data, 10, https://doi.org/10.1038/s41597-023-02549-6, 2023.

Didan, K.: MYD13A2 MODIS/Aqua Vegetation Indices 16-Day L3 Global 1km SIN Grid V006, Data set. NASA EOSDIS Land Processes Distributed Active Archive Center, https://doi.org/10.5067/MODIS/MYD13A2.006, Accessed 2024-03-19, 2015a.

Didan, K.: MOD13A2 MODIS/Terra Vegetation Indices 16-Day L3 Global 1km SIN Grid V006, Data set. NASA EOSDIS Land Processes Distributed Active Archive Center, https://doi.org/10.5067/MODIS/MOD13A2.006, Accessed 2024-03-19, 2015b.

Forkel, M., Drüke, M., Thurner, M., Dorigo, W., Schaphoff, S., Thonicke, K., Von Bloh, W., and Carvalhais, N.: Constraining modelled global vegetation dynamics and carbon turnover using multiple satellite observations, Scientific Reports, 9, 18 757, https://doi.org/10.1038/s41598-019-55187-7, 2019.

Harper, K. L., Lamarche, C., Hartley, A., Peylin, P., Ottlé, C., Bastrikov, V., San Martín, R., Bohnenstengel, S. I., Kirches, G., Boettcher, M., Shevchuk, R., Brockmann, C., and Defourny, P.: A 29-year time series of annual 300 m resolution plant-functional-type maps for climate models, Earth System Science Data, 15, 1465–1499, https://doi.org/10.5194/essd-15-1465-2023, 2023.

Hersbach, H., Bell, B., Berrisford, P., Biavati, G., Horányi, A., Muñoz Sabater, J., Nicolas, J., Peubey, C., Radu, R., Rozum, I., Schepers, D., Simmons, A., Soci, C., Dee, D., and Thépaut, J.-N.: ERA5 hourly data on single levels from 1940 to present, Copernicus Climate Change Service (C3S) Climate Data Store (CDS), https://doi.org/10.24381/cds.adbb2d47, accessed on 11-04-2024, 2023.

Lange, S., Mengel, M., Treu, S., and Büchner, M.: ISIMIP3a atmospheric climate input data (v1.0), https://doi.org/10.48364/ISIMIP.982724, iSIMIP Repository, 2022.

Monteith, J. L.: Evaporation and environment, in: Symposia of the society for experimental biology, vol. 19, pp. 205–234, Cambridge University Press (CUP) Cambridge, 1965.

Ruijsch, D., van Mourik, J., Biemans, H., Hauswirth, S. M., and Wanders, N.: Thrive or Wither: Exploring the Impacts of Multiyear Droughts on Vegetation, Journal of Geophysical Research: Biogeosciences, https://doi.org/10.1029/2025JG008992, 2025.

Running, S. W. and Zhao, M.: User's Guide: Daily GPP and Annual NPP (MOD17A2H/A3H) and Year-end Gap-Filled (MOD17A2HGF/A3HGF) Products: NASA Earth Observing System MODIS Land Algorithm (Collection 6.1), Numerical Terradynamic Simulation Group, University of Montana, https://www.umt.edu/numerical-terradynamic-simulation-group/project/modis/user-guides/mod17c61usersguidev11mar112021.pdf, 2021.

Tang, X., Li, H., Huang, N., Li, X., Xu, X., Ding, Z., and Xie, J.: A comprehensive assessment of MODIS-derived GPP for forest ecosystems using the site-level FLUXNET database, Environmental Earth Sciences, 74, 5907–5918, https://doi.org/10.1007/s12665-015-4615-0, 2015.

Vicente-Serrano, S., Beguería, S., and López-Moreno, J.: A Multiscalar Drought Index Sensitive to Global Warming: The Standardized Precipitation Evapotranspiration Index, Journal of Climate, 23, 1696–1718, https://doi.org/10.1175/2009JCLI2909.1, 2010.

Vremec, M., Collenteur, R. A., and Birk, S.: Technical note: Improved handling of potential evapotranspiration in hydrological studies with *PyEt*, Hydrology and Earth System Sciences Discussions, 2023, 1–23, https://doi.org/10.5194/hess-2022-417, 2023.

Wang, L., Zhu, H., Lin, A., Zou, L., Qin, W., and Du, Q.: Evaluation of the Latest MODIS GPP Products across Multiple Biomes Using Global Eddy Covariance Flux Data, Remote Sensing, 9, https://doi.org/10.3390/rs9050418, 2017.

Wang, S. and Zhang, Y.: Temporally corrected long-term satellite solar-induced chlorophyll fluorescence (SIF) dataset (1995-2018), https://doi.org/10.6084/m9.figshare.21546066.v1, 2023.

Zhu, X., Pei, Y., Zheng, Z., Dong, J., Zhang, Y., Wang, J., Chen, L., Doughty, R. B., Zhang, G., and Xiao, X.: Underestimates of Grassland Gross Primary Production in MODIS Standard Products, Remote Sensing, 10, https://doi.org/10.3390/rs10111771, 2018.

Zotarelli, L., Dukes, M. D., Romero, C. C., Migliaccio, K. W., and Morgan, K. T.: Step by Step Calculation of the Penman-Monteith Evapotranspiration (FAO-56 Method): AE459, 2/2010, EDIS, 2010, https://doi.org/10.32473/edis-ae459-2010, 2024.